

A Runge Kutta Discontinuous Galerkin approach to solve reactive flows on conforming hybrid grids.

G. Billet*, J. Ryan* and M. Borrel*
Corresponding author: billet@onera.fr

* ONERA, France.

Abstract: A Runge-Kutta Discontinuous Galerkin method (*RKDG*) to solve the parabolic and source parts of reactive Navier-Stokes equations written in conservation form is presented. The parabolic operator uses a recent recovery method set up by van Leer for structured grids and a new projection method proposed by Borrel-Ryan for unstructured grids. In a 1-D test case the *RKDG* method is compared with a high order finite difference method. A 2-D test case on hybrid mesh is presented.

Keywords: Discontinuous Galerkin approach; Runge-Kutta time scheme; reactive flows; multi-species flows; unsteady flows; gaseous interface; hybrid grid.

1 Introduction

In [1], we described a Runge-Kutta Discontinuous Galerkin (*RKDG*) method that solves the hyperbolic part of the reactive *NS* equations written in conservation form on regular Cartesian grids. Herein, we focus our attention on the parabolic and source terms of the reactive *NS* equations. The transport fluxes are expressed in terms of transport coefficients and macroscopic variable gradients. The transport coefficients are functions of the state of the mixture, i.e., of pressure, temperature and species mass fractions. The molar production rates are of Maxwellian type and are compatible with the law of mass action.

Nowadays, there exists two categories of methods to solve the parabolic terms. In the first category, schemes are devised through a mixed formulation by introducing an equation for the gradient that takes into account the jump of the solution at interfaces. These schemes need to be stabilized by either interior penalty terms or numerical viscosity terms with parameters to be adjusted. Depending on the formulation, the resulting scheme is either compact or non compact. Among the many contributors, we can cite Bassi and Rebay with their BR1 and BR2 methods for the compressible *NS* equations [2]-[3], Baumann and Oden [4], Cockburn and Shu with the LDG method [5], Peraire and Persson with the CDG method [6], Liu and Yan with the DDG method [7], Brezzi and al. [8]-[9] with the symmetric interior penalty (IP) method. In [10], Munz and al. show the link between their diffusive generalized Riemann solver and the IP approach.

The second category is based on local reconstruction or recovery of the solution to smooth the discontinuities. van Leer et al. [11]-[12] were the first to propose the so-called Recovery method where the viscous fluxes at element boundaries are computed by merging the adjacent elements and defining on this new element a locally smooth P^{2k+1} recovered solution that is in the weak sense indistinguishable from the piecewise discontinuous P^k solution. This method eliminates the artificial introduction of penalty terms and the tuning of parameters. This approach is very accurate and efficient on structured grids but an impediment is the construction of the local merging basis and the need to solve a linear problem at each interface which can be awkward if we use an adaptive strategy on unstructured grids. On unstructured grids, a simpler numerical procedure is chosen (*EDG* method) [13]. This method, previously presented in [14], is a sequel to the shift cell technique that uses the Green formula that reconstructs the gradient by projection on the shift cell basis. For 2-D simulations, the jumps across element boundaries are eliminated in the computation of the viscous fluxes using a projection of the piecewise P^k discontinuous solution on the P^k basis of the overlapping rectangular elements.

Diffusion phenomena are fundamental in reactive flows. Thus it is necessary to describe them with the best possible accuracy while maintaining compactness of the scheme. The Recovery method on structured meshes and the *EDG* method on the unstructured meshes satisfy these requirements and were chosen for this paper.

Because of the great number of equations, the expressions of the transport coefficients and the chemical reactions, it appears judicious to limit the method order to *DGP*² for reactive flows in order to have realistic computational costs. In the simulations, a third-order *TVD* Runge-Kutta *RK*³ scheme [15] is associated with a *DGP*² approach. The first case is a 1-D sinusoidal reactive mixing of mass and temperature where *RK*³*DGP*² is compared with a 6th order finite difference code [18]. The second test case uses a conforming hybrid grid representing a 2-D combustion chamber with a flame holder. Strong acoustic waves, flame fronts and gaseous detonations are observed.

2 Conservation equations

The equations governing multicomponent flows are derived from the kinetic theory of gases and express conservation of species mass, momentum, and energy [19, 20]. The parabolic and source parts of these equations may be written in the form

$$\begin{aligned}\partial_t(\rho Y_i) &= -\nabla \cdot (\rho Y_i V_i) + m_i \omega_i, & i \in \mathcal{N}_S \\ \partial_t(\rho \mathbb{V}) &= -\nabla \cdot \Pi \\ \partial_t(\rho E) &= -\nabla \cdot (q + \Pi \mathbb{V})\end{aligned}$$

with

$$\begin{aligned}\Pi &= -(\kappa - \frac{2}{3}\eta)(\nabla \cdot \mathbb{V})I - \eta(\nabla \mathbb{V} + (\nabla \mathbb{V})^t) \\ q &= \sum_{i \in \mathcal{N}_S} \rho h_i Y_i V_i - \lambda \nabla T + p \sum_{i \in \mathcal{N}_S} \chi_i V_i \\ \rho Y_i V_i &= - \sum_{j \in \mathcal{N}_S} \rho Y_i D_{ij} (d_j + \chi_j \nabla \log T) \\ d_i &= \nabla X_i + (X_i - Y_i) \nabla \log p\end{aligned}$$

where ∂_t and ∇ are the time and space derivative operators, ρ the density, Y_i and X_i the mass fraction and the molar fraction of the i^{th} species, $\mathbb{V} = (u, v, w)$ the hydrodynamic velocity, V_i and m_i the diffusion velocity and the molar weight of the i^{th} species, ω_i the molar production rate of the i^{th} species, $\mathcal{N}_S = \{1, \dots, n\}$ the species indexing set, n the number of species in the mixture, $E = \frac{1}{2} \mathbb{V} \cdot \mathbb{V} + e$ the total energy per unit mass where e is the internal energy per unit mass, T the absolute temperature, h_i the enthalpy per unit mass of the i^{th} species, q the heat flux vector, I the unit tensor and Π the viscous tensor. The pressure p is given by

$$p = \rho \mathcal{R} T \sum_{i \in \mathcal{N}_S} \frac{Y_i}{m_i}$$

where \mathcal{R} is the gas constant.

In this equation set, the transport coefficients are the shear viscosity η , the bulk viscosity κ , the thermal conductivity λ , the multicomponent diffusion coefficients (D_{ij}), $i, j \in \mathcal{N}_S$ and the thermal diffusion ratios χ_i , $i \in \mathcal{N}_S$. The transport coefficients are functions of the state of the mixture, i.e., of pressure, temperature and species mass fractions. The mass conservation constraint for the species diffusion velocities

$$\sum_{i \in \mathcal{N}_S} Y_i V_i = 0$$

is added (for more details, see [21]).

The present paper studying only the numerical behavior of the method, it is not necessary to introduce approximate expressions rigorously derived from the kinetic theory for the transport coefficients. Empirical expressions are introduced [20] to evaluate the shear viscosity η and the thermal conductivity λ

$$\eta = \frac{1}{2} \left[\sum_{i \in \mathcal{N}_S} \eta_i X_i + \frac{1}{\sum_{i \in \mathcal{N}_S} \frac{X_i}{\eta_i}} \right] \quad (1)$$

$$\lambda = \frac{1}{2} \left[\sum_{i \in \mathcal{N}_S} \lambda_i X_i + \frac{1}{\sum_{i \in \mathcal{N}_S} \frac{X_i}{\lambda_i}} \right]. \quad (2)$$

The pure species shear viscosities λ_i and thermal conductivities η_i take on the form of third-order polynomial approximations with respect to the temperature. For the same reason, the bulk viscosity is neglected and all the Lewis numbers Le_i are assumed equal to 1 to calculate the species diffusion velocities. This hypothesis gives for the diffusion coefficients the expression

$$D_{ij} = D = \frac{\lambda}{\rho C_P} = \frac{\lambda}{\rho \sum_{i \in \mathcal{N}_S} C_{P_i}(T) Y_i}$$

where $C_{P_i}(T)$ is the constant-pressure specific heat of species i . Ignoring the baro-diffusion term and the Soret and Dufour effects, the diffusion velocity V_i is

$$V_i = -D \frac{\nabla Y_i}{Y_i}. \quad (3)$$

The extension of *RKDG* to more accurate approximations of the transport coefficients is natural and does not present any numerical difficulties.

3 Chemistry

We consider a complex reaction mechanism involving an arbitrary number of elementary chemical reactions



where ν_{ki}^d and ν_{ki}^r are the direct and reverse stoichiometric coefficients of the k^{th} species in the i^{th} reaction, $\mathcal{R} = \{1, \dots, n^r\}$ is the reaction indexing set, n^r the number of chemical reactions, and \mathcal{X}_k is a symbol for the k^{th} species. The Maxwellian rate of production for the k^{th} species, as derived from the kinetic theory of gases, is given by

$$\omega_k = \sum_{i \in \mathcal{R}} \nu_{ki} r_i, \quad (4)$$

where $\nu_{ki} = \nu_{ki}^r - \nu_{ki}^d$ and r_i is the rate of progress of the i^{th} reaction. The rate of progress r_i is the difference between the direct and reverse rates

$$r_i = \mathcal{K}_i^d \prod_{k \in \mathcal{N}_S} \left(\frac{\rho_k}{m_k} \right)^{\nu_{ki}^d} - \mathcal{K}_i^r \prod_{k \in \mathcal{N}_S} \left(\frac{\rho_k}{m_k} \right)^{\nu_{ki}^r},$$

where ρ_k/m_k is the molar concentration of the k^{th} species and \mathcal{K}_i^d and \mathcal{K}_i^r are the direct and reverse reaction constants for the i^{th} reaction. The reaction constant \mathcal{K}_i^d is usually estimated by an Arrhenius expression whereas \mathcal{K}_i^r is evaluated from the relation $\mathcal{K}_i^d/\mathcal{K}_i^r = \mathcal{K}_i^e$ where \mathcal{K}_i^e is the equilibrium constant of the i^{th} reaction [20].

The *RK³DGP²* method devoted to reactive flows was first presented in [22] with a simplified reaction

mechanism involving 4 species and 2 reactions [23]. In this paper, this reaction mechanism is introduced in the 2-D simulation. For the 1-D simulation, the RK^3DGP^2 method is coupled with a detailed mechanism. This chemical reaction mechanism of hydrogen in air includes 9 species (H_2 , O_2 , H_2O , H_2O_2 , HO_2 , OH , H , O , N_2) and 19 elementary reversible reactions [24]. With this mechanism, some chemical processes are very stiff and when the reaction starts, it is necessary to limit the absolute variation of some chemical species, especially H_2O_2 and HO_2 , during each time step. During this stage, the time step δt is consequently driven by chemical reactions [18]-[21].

4 Operator splitting

The simulation of severe flow conditions, such as unsteady reactive supersonic flows, requires robust accurate numerical methods. We use an operator splitting technique with separate operators for convective terms, dissipative terms, and chemistry sources. The splitting can be written in the symbolic form

$$\mathcal{U}^{n+1} = \left(\mathcal{L}_S\left(\frac{\delta t}{3}\right) \mathcal{L}_P\left(\frac{\delta t}{3}\right) \mathcal{L}_H\left(\frac{\delta t}{3}\right) \right) \mathcal{U}^n \quad (5)$$

where \mathcal{L}_H is the hyperbolic operator, \mathcal{L}_P the parabolic operator, \mathcal{L}_S the source operator, and δt the physical time step. The hyperbolic operator has been described in [1]. The parabolic operator, which takes into account all dissipative effects and the source operator which represents the chemistry reactions are described in details below.

5 TVD-Runge-Kutta time discretization (RK^3)

For each spatial operator in Eq.(5), the previous semi-discrete scheme can be generalized as $\frac{1}{3}\partial_t(\mathcal{U}) = -\mathcal{L}_\phi(\mathcal{U})$ with $\phi = H, P$ and S . This scheme is discretized in time by a Runge-Kutta time discretization, e.g. the third-order version proposed by Shu and Osher [15]:

$$\begin{aligned} \mathcal{U}_j^{(l)\alpha} &= \mathcal{U}_j^{(l)n+\gamma} - \delta t \mathcal{L}_{\phi_j}^{(l)n+\gamma} \\ \mathcal{U}_j^{(l)\beta} &= \frac{3}{4}\mathcal{U}_j^{(l)n+\gamma} + \frac{1}{4}\mathcal{U}_j^{(l)\alpha} - \frac{\delta t}{4}\mathcal{L}_{\phi_j}^{(l)\alpha} \\ \mathcal{U}_j^{(l)n+\frac{1}{3}+\gamma} &= \frac{1}{3}\mathcal{U}_j^{(l)n+\gamma} + \frac{2}{3}\mathcal{U}_j^{(l)\beta} - \frac{2\delta t}{3}\mathcal{L}_{\phi_j}^{(l)\beta} \end{aligned} \quad (6)$$

where, $\mathcal{U}_j^{(l)}(t)$ is the l^{th} degree of freedom (*DOF*) in cell Ω_j and γ varies with the operator: $\gamma = 0$ for \mathcal{L}_H , $\gamma = \frac{1}{3}$ for \mathcal{L}_P and $\gamma = \frac{2}{3}$ for \mathcal{L}_S .

6 Discontinuous Galerkin (DGP^2)

The solution as well as the test function space is given by

$\mathcal{W}_h^k = \{\varphi \in L^\infty(\Omega) / \forall j, \varphi|_{\Omega_j} \in P^k(\Omega_j)\}$ where $P^k(\Omega_j)$ is the space of polynomials of degree $\leq k$ on the cell Ω_j , (in our case $k = 2$). We define a local orthogonal basis over Ω_j , $\{\phi_j^{(l)}(\mathbb{X}), l = 0, 1, \dots, k\}$ where $\phi_j^{(l)}(\mathbb{X})$ are the Legendre polynomials and $\mathbb{X} = (x, y, z)$. The numerical solution in the test function space \mathcal{W}_h^k is written as

$$\forall t \in [0, T], \forall \mathbb{X} \in \Omega_j, \mathcal{U}^h(\mathbb{X}, t) = \sum_{l=0}^{l=k} \mathcal{U}_j^{(l)}(t) \phi_j^{(l)}(\mathbb{X}) \text{ for } \mathbb{X} \in \Omega_j.$$

A weak formulation of the problem is obtained by multiplying the *NS* equations by a test function φ and by integrating on each cell Ω_j . Then, a discrete analogous is obtained by replacing the exact solution \mathcal{U} by the approximation $\mathcal{U}^h(\mathbb{X}, t)$, $\forall t \in [0, T], \forall j$,

$$\int_{\Omega_j} \varphi \partial_t(\mathcal{U}^h) d\Omega = - \int_{\Omega_j} \varphi (\nabla(\mathcal{F}^h)) d\Omega + \int_{\Omega_j} \varphi \mathcal{S}^h d\Omega.$$

The test function φ is replaced by each element of the basis set $\phi_j^{(l)}(\mathbb{X})$ and the transport fluxes \mathcal{F} are integrated by part. The source term \mathcal{S} represents the production rates of each species. The integral terms for DGP^2 method are evaluated using quadrature rules.

The stability condition for this scheme (see [16], [17]) is based on the following formula:

$$\Delta t = \min(\Delta t_H, \Delta t_P, \Delta t_S)$$

with

$$\begin{aligned} \Delta t_H &= Cfl \min\left(\frac{\Delta x}{|u|+c}, \frac{\Delta y}{|v|+c}\right) \\ \Delta t_P &= \min\left(\frac{\rho C_v \Delta x^2}{2\lambda}, \frac{\rho C_v \Delta y^2}{2\lambda}, D_0 \frac{Re \Delta x}{|u|+c}, D_0 \frac{Re \Delta y}{|v|+c}\right) \end{aligned}$$

where c is the sound velocity, C_v the constant-volume specific heat, Re is the Reynolds number based on the mesh size, Δt_S is given by the stiffness of reaction rates as in subsection 8.1, $Cfl = .2$ and $D_0 = .2$.

6.1 2-D Recovery method [12]

The extension of the Recovery [11] to 2-D and a fortiori to 3-D problems is not straightforward. The notion of directionality enters and the choice of the recovery basis becomes nontrivial. As in [12], we present the procedure in 2-D and for $k = 2$. We focus the study on interfaces $\partial\Omega_j$ and more particularly on the one located between Ω_j and Ω_{j+1} : $\Gamma_{j+1/2}$, (see Fig. 1).

We introduce the local coordinate system (ξ, η) located at the midpoint of the interface $\Gamma_{j+1/2}$. With a Cartesian grid, axis x et ξ have the same direction (id. for y and η). In order to keep in direction ξ the same basis than in 1-D $(1, \xi, \xi^2, \xi^3, \xi^4, \xi^5)$ [11] and to avoid a singular system, we add the elements $\eta, \eta\xi, \eta\xi^2, \eta\xi^3, \eta^2, \eta^2\xi$. This choice keeps the good properties of the recovery method set-up in 1-D in the normal direction ξ and preserves the same accuracy in the tangential direction η in the interval $-\Delta y/2$ and $\Delta y/2$. In 2-D and for $k = 2$, the approximated solution $\mathcal{V}^h(x, y)$ is expressed on $\Omega_R = \Omega_j \cup \Omega_{j+1}$ as

$$\begin{aligned} \mathcal{V}^h(\xi, \eta) &= \sum_{l=0}^{l=5} \mathcal{U}_j^{(l)}(t) \psi^{(l)}(\xi, \eta) + \sum_{l=0}^{l=5} \mathcal{U}_{j+1}^{(l)}(t) \psi^{(6+l)}(\xi, \eta) \\ \text{for } -\Delta x &\leq \xi \leq \Delta x \quad \text{et} \quad -\frac{\Delta y}{2} \leq \eta \leq \frac{\Delta y}{2}. \end{aligned}$$

Since only the values of $\mathcal{V}^h(0, y)$, $\mathcal{V}_x^h(0, y)$ and $\mathcal{V}_y^h(0, y)$ are useful, this approach is very economical because a lot of coefficients in the expressions of $\psi^{(l)}(\xi, \eta)$ cancel for $\xi = 0$ and the expressions of $\mathcal{V}^h(0, y)$, $\mathcal{V}_x^h(0, y)$ and $\mathcal{V}_y^h(0, y)$ depend only on the mean and jump operators of the degrees of freedom $\mathcal{U}_j^{(l)}$ and $\mathcal{U}_{j+1}^{(l)}$. With the following notations, for the average and the jump operators at interface $\Gamma_{j+1/2}$

$$\langle \bullet \rangle = \frac{(\bullet)_{j+1} + (\bullet)_j}{2}, \quad [\bullet] = (\bullet)_{j+1} - (\bullet)_j,$$

the approximation $\mathcal{V}^h(0, y)$ and its derivatives are expressed as

$$\begin{aligned} \mathcal{V}^h(0, y) &= \langle \mathcal{U} \rangle - \frac{13\Delta x}{64} [\mathcal{U}_x] + \lambda_y \frac{\Delta y}{2} \langle \mathcal{U}_y \rangle + \frac{7\Delta x^2}{192} \langle \mathcal{U}_{xx} \rangle - \lambda_y \frac{\Delta x \Delta y}{12} [\mathcal{U}_{xy}] + \frac{\Delta y^2}{8} (\lambda_y^2 - \frac{1}{3}) \langle \mathcal{U}_{yy} \rangle \\ \mathcal{V}_x^h(0, y) &= \frac{15}{4\Delta x} [\mathcal{U}] - \frac{11}{4} \langle \mathcal{U}_x \rangle + \lambda_y \frac{9\Delta y}{8\Delta x} [\mathcal{U}_y] + \frac{\Delta x}{10} [\mathcal{U}_{xx}] - \lambda_y \frac{5\Delta y}{8} \langle \mathcal{U}_{xy} \rangle + \frac{\Delta y^2}{8\Delta x} (\lambda_y^2 - \frac{1}{3}) [\mathcal{U}_{yy}] \\ \mathcal{V}_y^h(0, y) &= \langle \mathcal{U}_y \rangle - \frac{\Delta x}{6} [\mathcal{U}_{xy}] + \lambda_y \frac{\Delta y}{2} \langle \mathcal{U}_{yy} \rangle \end{aligned}$$

with $-1 \leq \lambda_y \leq 1$.

6.2 EDG method [13]

In the *EDG* method, a continuous solution is built locally through a L_2 projection of the discontinuous interface solution on a small rectangular overlapping interface element, named *Elastoplast*, with an orthogonal basis of the same order as the one in the neighboring cells. The main motivation for developing the *Elastoplast* method, is to devise a simpler numerical procedure easily implemented on unstructured grids. This method is described in detail in [13].

6.3 Particularities of the parabolic operator

To compute the temperature T and the gradient ∇T at Gauss points, we use Eq. (4) in [1]

$$T \sum_{i=1}^{N_s} \left(\frac{\mathcal{R}}{b_i^m} - \frac{\mathcal{R}}{m_i} \right) \rho Y_i = \rho E - \rho h_0^m - \frac{\rho \nabla^2}{2}.$$

The gradient ∇T is then obtained from the conservative quantity gradients. At the end of the Runge-Kutta procedure on the parabolic operator, the constraint associated with the mass fractions is applied [1]

$$\sum_{i \in S} (\rho Y_i^{(0)})^{n+2/3} = (\rho^{(0)})^{n+2/3} = (\rho^{(0)})^{n+1/3}.$$

6.4 Particularities of the source operator

Operator \mathcal{L}_S solves

$$\partial_t(\rho Y_i) = m_i \omega_i$$

with the constraint $\sum_{i=1}^{N_s} m_i \omega_i = 0$. Generally, to verify this last equality, it is necessary to add the following relation after computing ω_i^c from Eq. (4)

$$\omega_i = \omega_i^c - |\omega_i^c| \frac{\sum_{j=1}^{N_s} m_j \omega_j^c}{\sum_{j=1}^{N_s} |m_j \omega_j^c|}.$$

Because of the strong variations of the mass fractions when the source operator is called, the constraints associated with the mass fractions is applied on all the degrees of freedom of the density at the end of the Runge-Kutta time step of the source operator

$$(\rho^{(l)})^{n+1} = \sum_{i \in S} (\rho Y_i^{(l)})^{n+1} \quad \text{for } l = k, k-1, \dots, 0.$$

7 High-order finite difference code (*FD6*)

The accuracy study is generally not easy with complicated physical phenomena, even in 1-D. The alternative is to compare the results with those obtained by a higher order method. The $RK^3 DGP^2$ method is compared with a high order finite difference method used in the *DNS* code *Parcomb* [18] developed at *ONERA* and *ECP* to investigate the interactions of turbulent flames with acoustic waves. *Parcomb* is a finite difference three-dimensional code solving the fully compressible *NS* equations for reacting flows. Derivatives are computed using centered explicit schemes of order six. The skew-symmetric splitting formulation of the non-linear terms proposed in [25] is implemented and a sixth-order explicit filter is used to stabilize the solution. The temporal integration is realized with a Runge-Kutta algorithm of order four. With these improvements, the stability domain reaches $Cfl = 1.5$ for the hyperbolic part of the *NS* equations. Chemical reaction schemes and transport coefficients are computed with standard methods similar to what is found

in the packages CHEMKIN II and TRANSPORT of Sandia National Laboratories. Comparisons between RK^3DGP^2 and $FD6$ concern only the numerical scheme, thus the same expressions of κ and λ are used (Eqs.(1),(2)) in $FD6$, the Lewis numbers are equal to 1 (Eq. (3)), the baro-diffusion effect, the Soret and Dufour effects as also the bulk viscosity are neglected. The chemical reaction mechanism is the same [24].

8 Numerical examples

After some comparisons in [1] between $RKDG$ and a $MUSCL$ approach and between RK^3DGP^1 and RK^3DGP^2 in [22], RK^3DGP^2 is confronted in this paper with a higher accurate scheme ($FD6$) in a reactive 1-D simulation. A numerical study of the error is realized for this case. A 2-D test case is also proposed. This is a reactive flow in a hybrid grid representing a rectangular chamber with a 'triangular' flame holder. The triangular unstructured grids are created with *Gmsh* [26].

In some cases, RK^3DGP^2 needs to call a limiting process [1]. For each test case, we indicate if the limiting process is called or not.

8.1 1-D reactive sinusoidal mixing H_2-O_2

We propose to study the reactive flow for a variable mixture of hydrogen-oxygen in a nitrogen medium and subjected to a variable temperature field. The domain dimension is $L = 40mm$. The boundary conditions are periodic. The mixture wave length $L_{Y_i} = L/4$.

With the hyperbolic operator, the process of limitation presented in [1] is applied but only on the ρY_i and with the most refined grids ($L_{Y_i} \geq 100$ cells) (see table 1). It is due to the brutal appearance of radicals which creates intense gradients on some mass fractions when the grid becomes very fine. The initial conditions are (see Fig. 2):

$$\begin{aligned} Y_{H_2} &= 0.015(1 - \sin 8\pi x/L) \\ Y_{O_2} &= 0.117(1 + \sin 8\pi x/L) \\ Y_{N_2} &= 1 - Y_{O_2} - Y_{H_2} \\ T(K) &= 850 - 550 \sin 2\pi x/L \\ u(m/s) &= 0. \\ p(atm.) &= 1. \end{aligned}$$

The simulations are carried out with various grids going from $L_{Y_i} = 5$ cells to $L_{Y_i} = 500$ cells. The solution obtained with $FD6$ for the thermochemical variables (temperature and mass fractions) changes little above $L_{Y_i} = 100$ cells. On the other hand, for the velocity and the pressure, it is necessary to refine up to $L_{Y_i} = 500$ cells. Beyond that, the solution barely changes. The simulation obtained with $FD6$ and $L_{Y_i} = 500$ cells will be used as reference solution ('exact' solution).

Here, the time step is no longer associated with the criterion of stability of the hyperbolic or parabolic operators but is controlled by the source operator and more particularly by the stiffest reactions of the chemical scheme. This time step is fixed at $\delta t = 4. \times 10^{-9}s$ at the beginning of simulations what corresponds to values of Cfl rather small ($Cfl = 0.002$ for the coarsest grid and $Cfl = 0.2$ for the finest grid). Flame fronts appear quickly where the temperature is initially high. Simulations are stopped at $t = 5. \times 10^{-4}s$, that is to say after more 10^5 time steps.

On sufficiently refined grids, the two methods RK^3DGP^2 (with $L_{Y_i} = 50$ cells) and $FD6$ (with $L_{Y_i} = 100$ cells) are quite similar to the 'exact' solution, as can be seen with the density (Fig. 3(a)). The results also show a very good agreement of temperature and mass fractions (Figs. 3(b), 3(c)) (for a better reading of the results, the *too close* 'exact' solution was not plotted). The velocity field (Fig. 3(d)), produced for the most part by the successive appearance of flame fronts, is strongly unsteady contrary to the previous fields which have a space evolution clearly less marked than their time evolution. The velocity field shows slight differences but both methods reproduce globally in phase and in amplitude the whole of the physical fluctuations. Nevertheless a weak space shift is visible with $FD6$ ($L_{Y_i} = 100$ cells) whereas the solution with RK^3DGP^2 ($L_{Y_i} = 50$ cells) is overall closer to the 'exact' solution.

The simulation, carried out on a slightly less refined grid ($L_{Y_i} = 25$ cells), begins to present some differences. *FD6* does not preserve as well the temperature profile as *RK³DGP²*, in particular on the left reactive zone where the maximum temperature is much too high with *FD6* (Fig. 4(a)). This problem could come from an important numerical diffusion or from the appearance of numerical instabilities when the wavelengths associated with mass fractions are not represented by a sufficient number of cells. The same problem appears for the mass fraction of water vapor. The water vapor production in the left flame is too important with *FD6* (Fig. 4(b)).

The velocity field is plotted for three grids. *FD6* develops numerical oscillations as soon as the grid is not sufficiently refined ($L_{Y_i} \leq 50$ cells) (Fig. 5(a)). On the other hand, *RK³DGP²* does not set up any instability and captures the whole of the fluctuations, without phase error (Fig. 5(b)) except with the coarser grid.

The relative errors with the L_1 norm on the temperature and the absolute value of the velocity are plotted on Figs. 6(a), 6(b) for six different grids at $t = 5 \times 10^{-4} s$. For $5 \text{ cells} \leq L_{Y_i} \leq 25 \text{ cells}$, the very high error on $|u|$ with *FD6*, due to the appearance of phase errors on velocity (Fig. 5(a)), causes a slope discontinuity at $L_{Y_i} = 50$ cells. For the coarsest grids ($5 \text{ cells} \leq L_{Y_i} \leq 50 \text{ cells}$) the error is weaker for T with *RK³DGP²* than with *FD6*. For these grids, no limitation is applied with *RK³DGP²*. With the finest grids, a limiting process is applied to the mass fractions for *RK³DGP²* otherwise simulations become unstable.

If comparisons are done not according to the grid but according to the number of degrees of freedom N_{DOF} per wave length L_{Y_i} , the curves of error for T are close until $N_{DOF} = 150$ (green filled squares for *RK³DGP²* and red circles for *FD6* on Fig. 6(a)). For $N_{DOF} \geq 200$, the curves diverge for two reasons. First, the limitation process is called for *RK³DGP²* and secondly, the error being based on the 'exact' solution (the solution obtained with *FD6* on a very refined grid), it is logical that the error associated with *FD6* tends more quickly towards zero than that of *RK³DGP²*.

8.2 Idealized combustion chamber with a conforming hybrid grid

With its hybrid grid, this simulation studies the behavior of the method around the interface separating the structured mesh where the parabolic terms are solved with the Recovery method [12] and the unstructured grid where the parabolic terms are treated with the *EDG* approach [13]. The Recovery method is applied only with Cartesian grid because it has the advantage of being accurate and fast for this kind of mesh. With the unstructured meshes, this method becomes too expensive and it is preferable to use faster methods such as the *EDG* approach. Hyperbolic terms for the unstructured meshes are treated the same way as in [13].

The reactive phenomena in a 2-D combustion chamber are simulated. The chamber geometry is presented in Fig. 7(a) with a relatively coarse grid ($\Delta x = \Delta y = 2.5 \text{ mm}$ in the Cartesian mesh). A 'triangular' shape flame holder is placed close to a premixed subsonic jet ($M = 0.32$). This case presents great constraints on the fields (strong and fast variations of the variables) especially close to the interface between structured and non-structured meshes. With this simulation presenting many stiff phenomena, robustness of the scheme and the discretization coupling can be evaluated in detail.

The domain dimensions are $L^2 = 8 \text{ cm} \times 16 \text{ cm}$. The inlet gaseous jet is defined at $t = 0$, for $y = 0$ and $3.5 \text{ cm} \leq x \leq 4.5 \text{ cm}$,

$$\begin{aligned}
 u &= 0 \text{ m/s} \\
 v &= 200 \text{ m/s} \\
 p &= 1 \text{ atm.} \\
 T &= 600 \text{ K} \\
 Y_{H_2} &= 0.04 \\
 Y_{O_2} &= 0.233 \\
 Y_{N_2} &= 0.727.
 \end{aligned}$$

This inlet flow is treated with *NSCBC* conditions [29] solved with a finite difference scheme. An outlet section is imposed at $y = 16 \text{ cm}$. This exit condition is solved with no reflection conditions. Everywhere else, the boundaries are represented by a wall with a no-slip condition and a temperature that remains fixed at $T = 300 \text{ K}$ on the chamber walls and at $T = 1000 \text{ K}$ for the flame holder walls. At $t = 0$, the flow in the chamber is at rest and temperature and pressure are uniform ($T = 300 \text{ K}$ and $p = 1 \text{ atm.}$). The grid

is composed of 1792 regular Cartesian cells and 570 unstructured elements. Thanks to the compactness of the *DG* method, overlapping grids are not needed and the physical transfers from one domain to the other one are calculated solely from the flux exchanges across the interfaces I_b separating the structured and unstructured grids (Fig. 10(b)). The time step corresponds to a $Cfl = 0.15$. At the end of the RK^3 scheme associated with the source operator, a limiting process (Cockburn’s limiter) is applied to the mass fractions for both discretizations. For the other quantities (mass, momentum and energy), this process is activated only once every one hundred time steps at the end of the hyperbolic operator.

At the beginning of the simulation, the jet circumvents the walls of the flame holder and is split into two flows (Fig. 7(b)). When the mixing fills the chamber, the reactive processes are generated by a heat release (idealized spark) at $t = 4.7 \times 10^{-3}s$ during a short time ($\Delta t = 3 \times 10^{-4}s$) at the location ($x = 4cm, y = 3cm$) (Fig. 7(a)). Just after the ignition, the numerical solution is presented at $t = 5.5 \times 10^{-3}s$ in Fig. 7(c).

From $t = 5.6 \times 10^{-3}s$, a strong coupling between the acoustic field and the reactive process appears. The transverse acoustic waves destabilize the jet and cause the successive set-up of three detonation waves near the entrance of fresh gases ($y = 0$ and $3.5cm \leq x \leq 4.5cm$). The set-up of the third gaseous detonation is presented in Figs. 8(a)-8(c). The phenomena associated with the detonation is shown between $t = 7.3 \times 10^{-3}s$ and $t = 7.6 \times 10^{-3}s$ on Figs. 9(a)-9(c). The Mach number and the pressure reach respectively 1.8 and 14 *atm.* during the appearance of the detonation waves. In these areas, the coupling of a finite difference scheme used to solve the *NSCBC* conditions for the inlet jet and the *DG* approach everywhere else is quite stable.

After the disappearance of the detonation waves, the flame hangs to the entering fresh gas and is stabilized (Fig. 10(a)). The numerical solution of the water vapor mass fraction is represented at the interfaces separating the structured and unstructured grids (Fig. 10(b)). No numerical instability appears in this region during the simulation.

9 Conclusion

A *RKDG* approach with no restrictive physical hypothesis has been developed for reactive flows. For this study, we used empirical but sufficient approximations of transport coefficients to show the capacities of this new method. Applying this approach with more sophisticated models is straightforward.

Comparisons on a 1-D simulation with a sixth order finite difference code with detailed kinetic scheme shows the good behavior of the presented approach particularly concerning its accuracy. RK^3DGP^2 seems stable and robust (even when this approach is coupled with a FD scheme) on 2-D hybrid grids. The only parameter of this method is the activation or not of the limiting process. Regarding a desired error level versus a given CPU time, it turns out to be more efficient to compute as much as possible on Cartesian meshes and to reserve the computation on unstructured ones only for the regions located close to irregular shaped walls. Extension to three-dimensional flows with non conforming hybrid grids is under development.

References

- [1] G. Billet and J. Ryan 'A Runge Kutta Discontinuous Galerkin approach to solve reactive flows: the hyperbolic operator.' *J. Comput. Phys.* 230(1), (2011).
- [2] F. Bassi and S. Rebay 'A high-order accurate discontinuous finite element method for the numerical solution of the compressible Navier-Stokes equations' *J. Comput. Phys.* 131, (1997).
- [3] F. Bassi, A. Crivellini, A. Di Pietro and S. Rebay 'An artificial compressibility flux for the discontinuous Galerkin solution of the incompressible Navier-Stokes equations' *J. Comput. Phys.* 218, (2006).
- [4] C. E. Baumann and J. T. Oden 'A discontinuous hp finite element method for convection-diffusion problems' *Computer Methods in Applied Mechanics and Engineering*, 175, (1999).
- [5] B. Cockburn and C.W. Shu 'Runge-Kutta discontinuous Galerkin methods for time-dependent convection-diffusion systems', *SIAM J. Numer. Anal.*, 35, pp2440-2463, (1998).
- [6] J. Peraire and P.O. Persson 'The compact discontinuous Galerkin (CDG) method for elliptic problems', *SIAM J. Sci. Comput.*, 30, pp1806-1824, (2008).

- [7] H. Liu and J. Yan 'The Direct Discontinuous Galerkin (DDG) methods for diffusion problems' *SIAM J. Numer. Anal.*, 47, (2009).
- [8] J. Douglas, Jr. and T. Dupont 'Interior penalty procedures for elliptic and parabolic Galerkin methods', *Lectures Notes in Phys.*, 58, pp207-216, (1976).
- [9] F. Brezzi, G. Manzini, D. Marini, P. Pietra and A. Russo 'Discontinuous Galerkin approximations for elliptic problems' *Numer. Meth. for Partial Diff. Eqns.*, 16, pp365-378, (2000).
- [10] G. Gassner, F. Lörcher and C.D. Munz 'A contribution to the construction of diffusion fluxes for finite volume and Discontinuous Galerkin schemes', *J. Comput. Phys.*, 224, pp1049-1064, (2007).
- [11] M. van Raalte and B. van Leer 'Bilinear forms for the recovery-based discontinuous Galerkin method for diffusion' *Proceedings ICFD 2007*, (2007).
- [12] B. van Leer, M. Lo and M. van Raalte 'A discontinuous Galerkin method for diffusion based on recovery' *18th AIAA CFD conference*, (2007).
- [13] J. Ryan and M. Borrel 'The Elastoplast Discontinuous Galerkin (EDG) method for the Navier-Stokes equations' *J. Comput. Phys.*, 231(1), (2012).
- [14] M. Borrel and J. Ryan 'A new discontinuous Galerkin method for the Navier-Stokes equations' *Proceedings of the ICOSAHOM09, Trondheim (Norway)*, June 22-26 2009, to appear in Lecture Notes in Comp. Sci. and Eng. Springer Ed.
- [15] C-W. Shu and S. Osher 'Efficient implementation of essentially non-oscillatory shock-capturing schemes' *J. Comput. Phys.*, 77, (1998).
- [16] C. Drozo, M. Borrel and A. Lerat 'Discontinuous Galerkin Schemes for the Compressible Navier-Stokes Equations' *Lecture Notes in Physics*, Vol.515 (1998).
- [17] G. Billet 'Improvement of convective concentration fluxes in a one step reactive flow solver', *J. Comput. Phys.*, 204, (2004).
- [18] A. Laverdant, L. Gouarin and D. Thevenin 'Interaction of a Gaussian wave with a turbulent non-premixed flame', *Comb. Theory & Mod.*, 11, pp585-602, (2007).
- [19] F. A. Williams 'Combustion theory' *Menlo Park, Benjamin/Cummings*, (1985).
- [20] V. Giovangigli 'Multicomponent flow modeling' *Birkhauser*, Boston, (1999).
- [21] G. Billet, V. Giovangigli and G. de Gassowski 'Impact of Volume Viscosity on a Shock-Hydrogen Bubble Interaction' *Comb. Theory & Mod.*, 12, pp221-248, (2008).
- [22] G. Billet and J. Ryan 'Runge Kutta Discontinuous Galerkin to solve reactive flows.' *Computational Fluid Dynamics 2010*, Editor A. Kuzmin, Springer, (2010).
- [23] R. C. Rogers and W. Chinitz 'Using a global hydrogen-air combustion model in turbulent reacting flow calculations' *AIAA journal*, Vol.21, n4, (1983).
- [24] J.A. Miller, R.E. Mitchell, M.D. Smooke and R.J. Kee, 'Toward a comprehensive chemical kinetic mechanism for the oxidation of acetylene: comparison of model predictions with results from flame and shock tube experiments', *19th symposium on combustion*, Combustion Institute, pp181-196, (1982).
- [25] A.E. Honein and P. Moin 'Higher entropy conservation and numerical stability of compressible turbulence simulations' *J. Comput. Phys.*, 201, (2004).
- [26] C. Geuzaine and J.F. Remacle 'Gmsh: a three-dimensional finite element mesh generator with built-in pre- and post-processing facilities', *Int. J. for Num. Meth. in Eng.*, pp1309-1331, (2009).
- [27] L. Krivodonova 'Limiters for high-order discontinuous Galerkin methods' *J. Comput. Phys.*, 226, pp276-296, (2007).
- [28] B. Cockburn and C-W. Shu, 'The Runge-Kutta discontinuous Galerkin finite element method for conservation laws V: Multidimensional systems', *J. Comput. Phys.*, 141, pp199-224, (1998).
- [29] M. Baum, T. Poinso and D. Thévenin 'Accurate boundary conditions for multicomponent reactive flows', *J. Comput. Phys.*, 116, pp247-261, (1994).

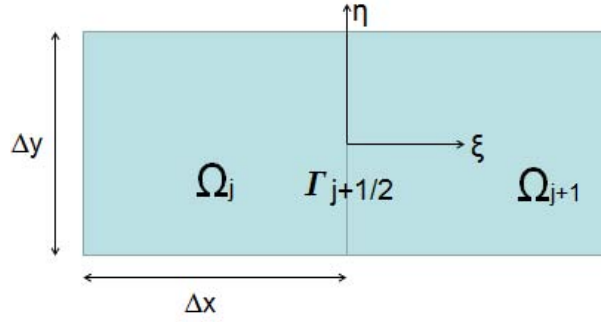


Figure 1: 2-D Recovery.

elements in domain L	20	40	100	200	400	1000
elements per wavelength L_{Y_i}	5	10	25	50	100	250
limiter (Krivodonova [27])	×	×	×	×	ρY_i	ρY_i

Table 1: Activation of the limiting process for the different grids.

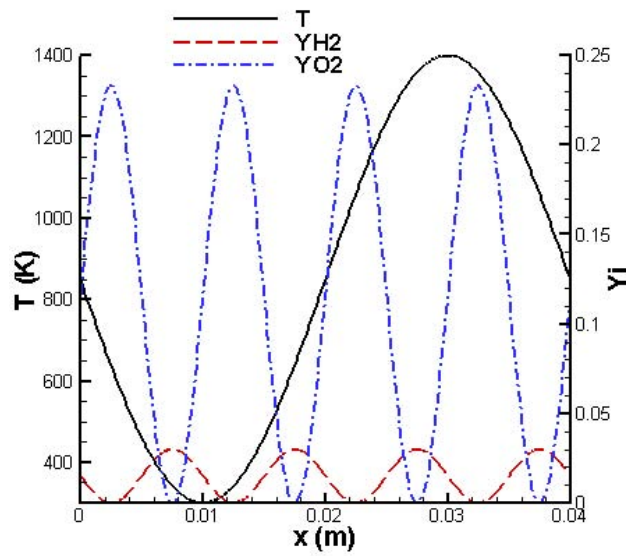
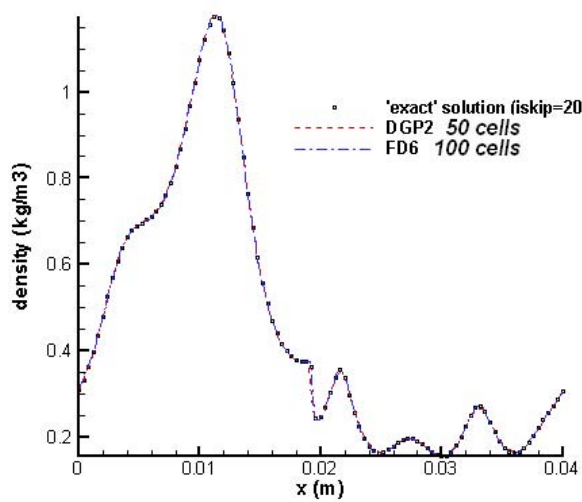
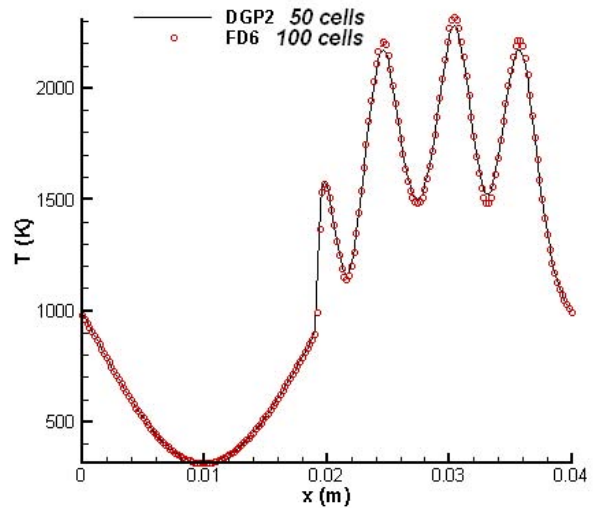


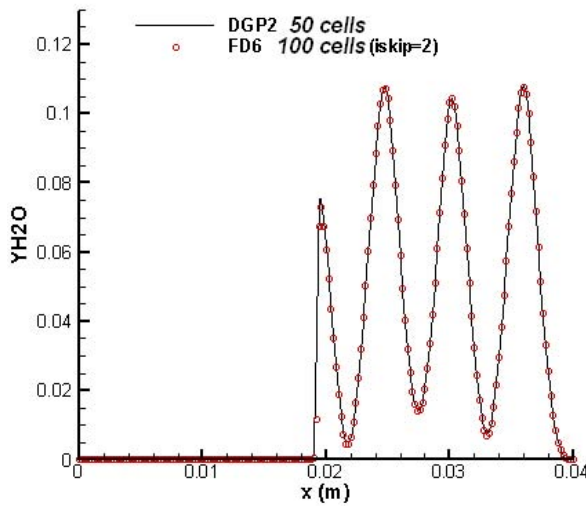
Figure 2: Initial mass fractions and temperature.



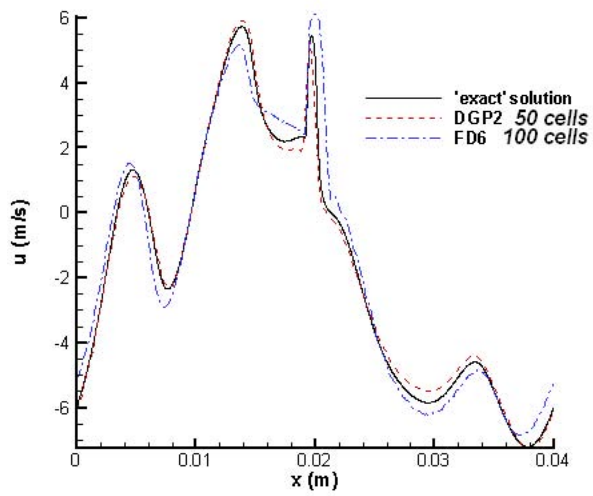
(a) Density field.



(b) Temperature field.

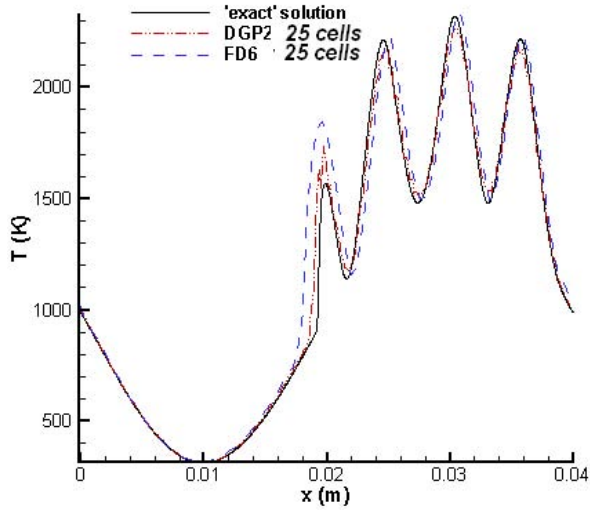


(c) Water vapor mass fraction.

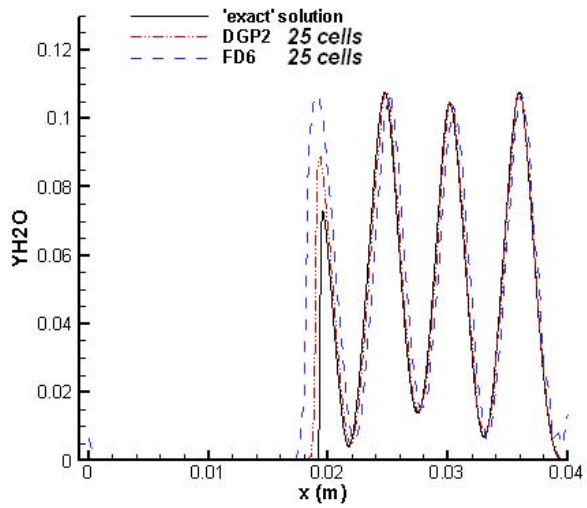


(d) Velocity field.

Figure 3: Density, temperature, water vapor and velocity with RK^3DGP^2 and $FD6$ at $t = 5 \times 10^{-4}$ s with fine meshes ($L_{Y_i} = 50$ cells and 100 cells) and comparisons with the 'exact' solution for density and velocity.

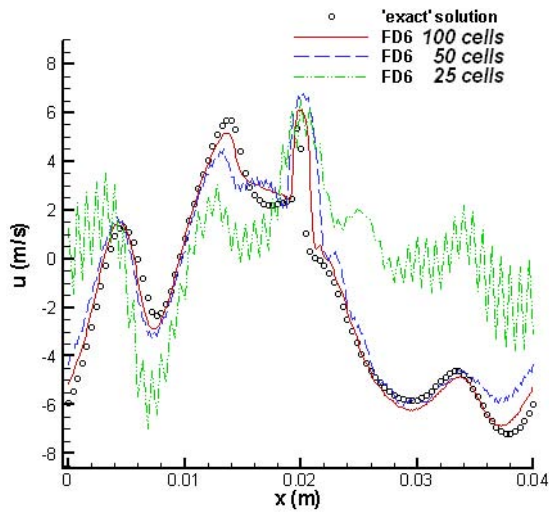


(a) Temperature.

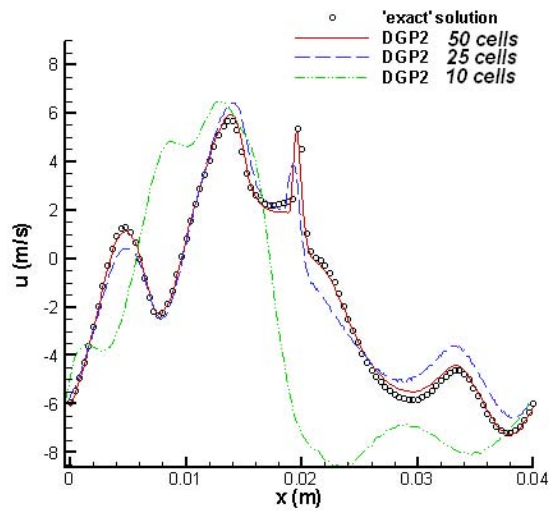


(b) Water vapor mass fraction.

Figure 4: Temperature and water vapor with RK^3DGP^2 and $FD6$ at $t = 5 \times 10^{-4}$ s with a coarse mesh ($L_{Y_i} = 25$ cells).

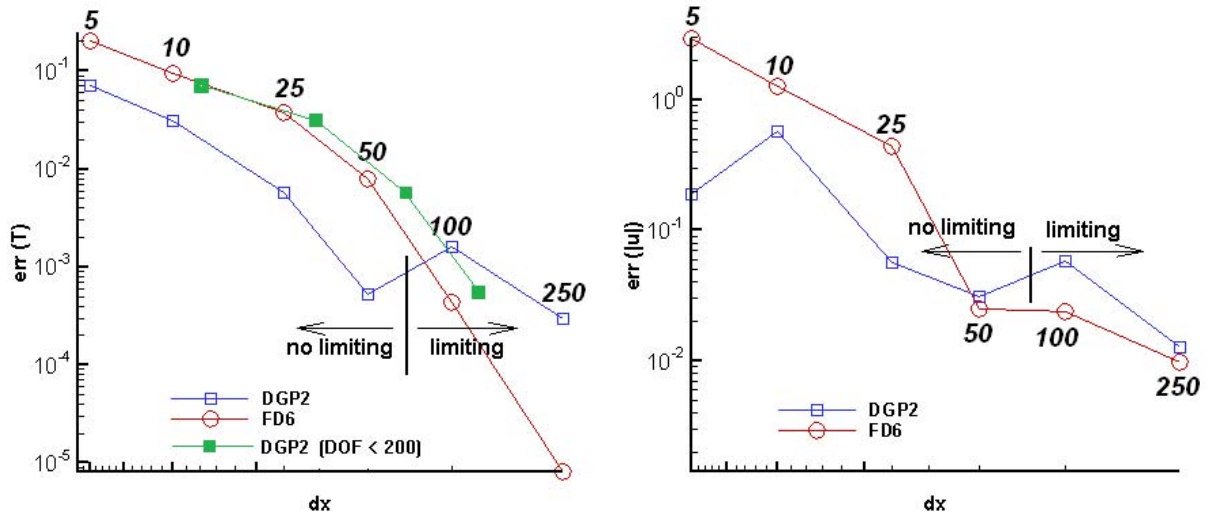


(a) $FD6$.



(b) RK^3DGP^2 .

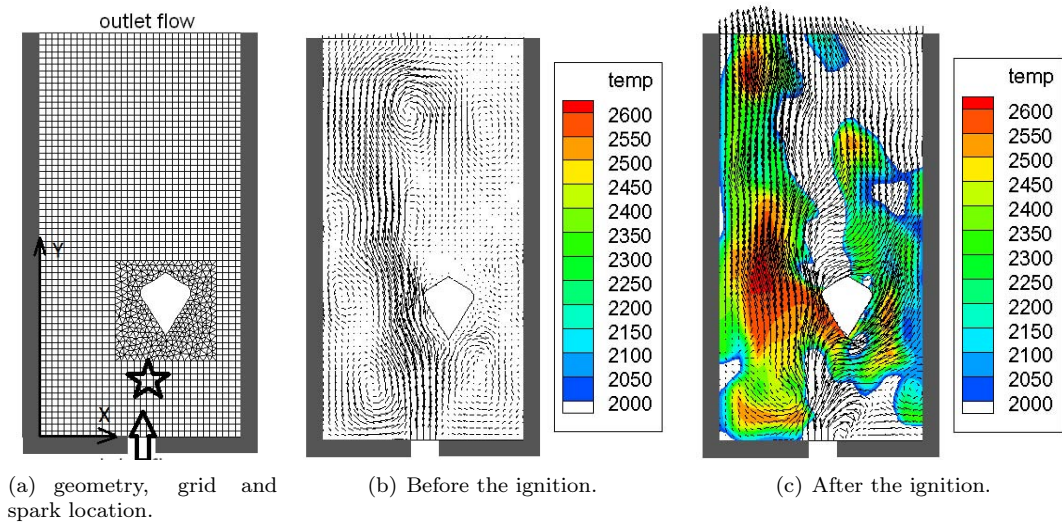
Figure 5: Velocity fields with RK^3DGP^2 and $FD6$ at $t = 5 \times 10^{-4}$ s for different meshes.



(a) Temperature error versus the grid refinement and the number of DOF .

(b) Velocity modulus error versus the grid refinement.

Figure 6: Relative error with L_1 norm at $t = 5 \times 10^{-4} s$ (the vertical bar separating the solution with and without limiting relates to only $RK^3 DGP^2$).



(a) geometry, grid and spark location.

(b) Before the ignition.

(c) After the ignition.

Figure 7: Geometry, grid and velocity and temperature fields before ($t = 4.5 \times 10^{-3} s$) and after ($t = 5.5 \times 10^{-3} s$) the ignition.

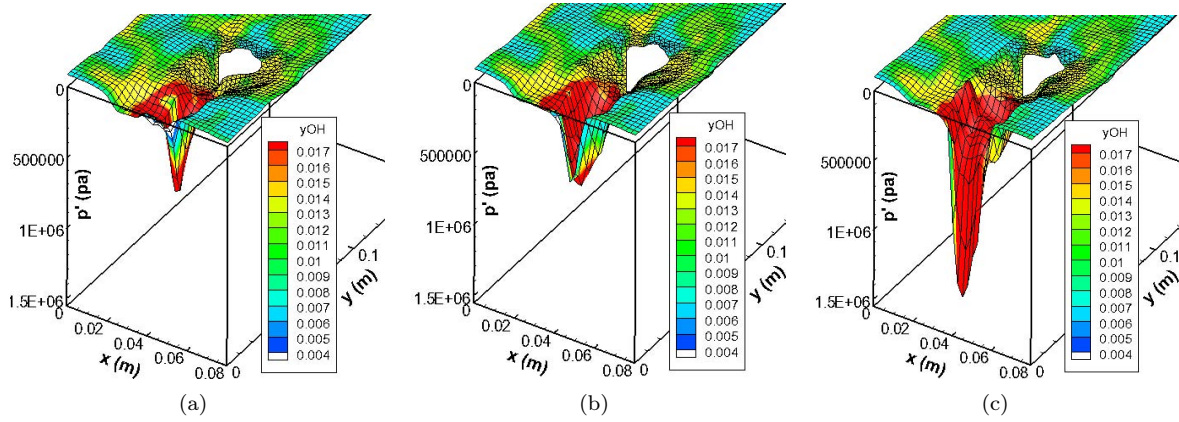
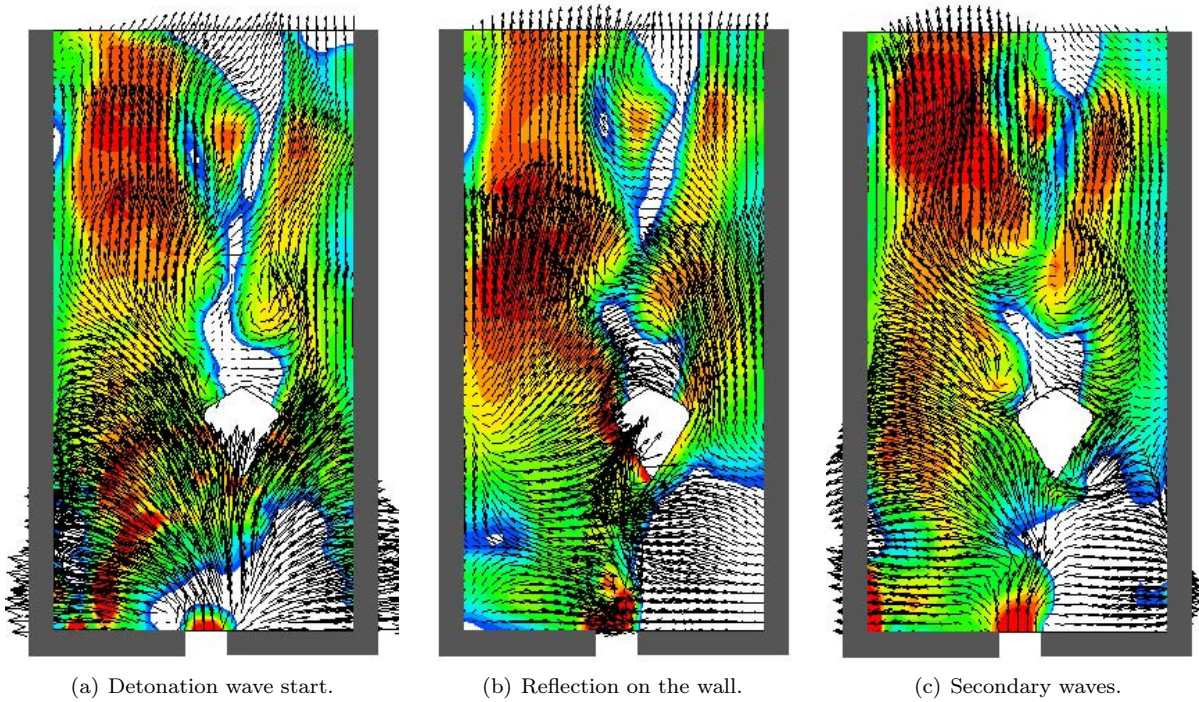


Figure 8: Detonation wave start. Pressure and hydroxide mass fraction fields.



(a) Detonation wave start.

(b) Reflection on the wall.

(c) Secondary waves.

Figure 9: Velocity and temperature just after the set-up of the third detonation wave (see Legend for the temperature in Fig. 7(c)).

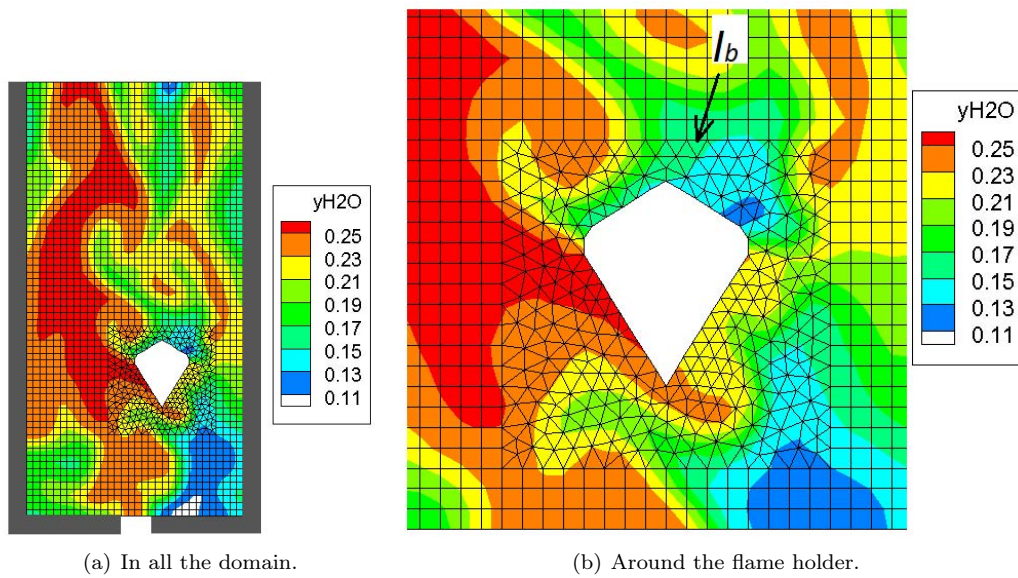


Figure 10: Water vapor mass fraction.